Ab initio study of the BaTiO_{3}/Ge interface

Mehmet Dogan and Sohrab Ismail-Beigi

Phys. Rev. B **96**, 075301 — Published 1 August 2017

DOI: 10.1103/PhysRevB.96.075301

Ab initio study of the $BaTiO_3$/Ge interface

Mehmet Dogan[1,2] and Sohrab Ismail-Beigi[1,2,3,4]
[1] *Center for Research on Interface Structures and Phenomena, Yale University, New Haven, Connecticut 06520, USA*
[2] *Department of Physics, Yale University, New Haven, Connecticut 06520, USA*
[3] *Department of Applied Physics, Yale University, New Haven, Connecticut 06520, USA*
[4] *Department of Mechanical Engineering and Materials Science, Yale University, New Haven, Connecticut 06520, USA*

We present a comprehensive first-principles study of $BaTiO_3$ ultrathin films epitaxially grown on Ge(001). We recently reported on the experimental realization of this system and analyzed the 2×1 structural distortions in the BTO thin film which may give rise to technologically relevant functional properties (D. P. Kumah, M. Dogan et al., *Phys. Rev. Lett.* **116**, 106101 (2016) [1]). In this work, we describe the structural and electronic properties of the experimentally observed interface configuration, as well as a distinct metastable interface configuration with a higher out-of-plane polarization. We show that these two distinct interface structures can be made energetically degenerate by choosing a top electrode with an appropriate work function, thus enabling, in principle, an epitaxial ferroelectric thin film oxide. We analyze the interface chemistry and electronic structure, and show that in the two polarization states the bands align differently, indicating a strong ferroelectric field effect. We also show that, surprisingly, in the intrinsic limit for the semiconductor, switching the oxide polarization state can cause the dominant charge carrier to switch between electrons and holes. The coupling of ferroelectric switching in the oxide with charge carrier type modulation in the semiconductor may have novel technological applications.

I. INTRODUCTION

Perovskite oxides have long been of great interest because of a large variety of phenomena that can emerge in these materials, such as ferroelectricity, ferromagnetism and superconductivity [2]. The phenomena give rise to technological utilization of these materials ranging from memory to photovoltaics [3]. Epitaxially growing oxides on semiconductors with an abrupt interface opens up possibilities for device applications with enhanced functionalities [4–7]. In the absence of interfacial amorphous layers (such as SiO_2), the mechanical and electrical properties of the semiconductor and the crystalline oxide can couple directly. Since the achievement of the first interface of this type between strontium titanate and silicon [8], $SrTiO_3$ has been used as a template for epitaxial growth of other oxides on Si [9–12] and Ge [13, 14]. With a high dielectric constant, STO was considered a promising candidate for a gate dielectric to replace SiO_2 [15] until it became clear that band alignment between Si and STO does not favor an insulating state for the thin oxide [16, 17]. However, because of potential applications of oxide/semiconductor systems in which a non-zero current through the oxide is desired, such as tunnel junctions, STO/Si heterostructures are still an active area of research.

Another motivating factor for studying STO thin films has been the possibility of inducing ferroelectricity in these films through epitaxial strain [18]. A ferroelectric insulating oxide that has a crystalline interface with a semiconductor forms the basis of ferroelectric field effect transistors (FEFET). In such a device, the polarization of the oxide can be switched by the application of a gate voltage, which in turn modifies the transport properties of the semiconductor underneath. Therefore the state of the device is encoded in the polarization of the ferroelectric oxide and does not require the continuous application of a gate voltage, which makes a FEFET non-volatile. Achieving non-volatile transistors would dramatically decrease the energy consumption of a wide variety of devices, and has been an important research goal for decades [19]. Barium titanate is an excellent candidate for this application because of its multitude of ferroelectric phases in the bulk and its high dielectric constant [20].

$BaTiO_3$ has been successfully grown on Si [7, 21, 22]; however in these studies $SrTiO_3$ has been used as a buffer layer due to the high lattice mismatch between Si and BTO of $\sim 4\%$. On the other hand, germanium closely matches the lattice constant of BTO within 1%, which has prompted many studies of BTO/Ge heterostructures [4, 13, 14, 23–25]. Some of these studies have included direct epitaxial interfaces between Ge and BTO without buffer layers; but a report on the atomic structure of this interface has only recently been published [1]. In this recent study, we reported on the epitaxial growth of ultrathin BTO films (2.5 & 5.5 unit cells) on Ge(001) surface. We presented a detailed analysis of the interface-induced 2×1 structural distortions in the oxide film which are associated with charge, spin and orbital order effects [26, 27]. In this current work, we complement our initial report with a comprehensive first-principles study of the structure of thin BTO films on Ge(001). In section III B we describe the atomic configurations of the various stable phases; in section III C we analyze the chemistry of the semiconductor-oxide interface, and the resulting elec-

tronic structure and band alignments throughout the system; in section III D we describe the ionic polarization in the oxide film; and in section III E we discuss oxygen content and how the film is stabilized on Ge with a high quality non oxygenated interface.

II. METHODS

We use density functional theory (DFT) with the Perdew–Burke–Ernzerhof generalized gradient approximation (PBE GGA) [28] and ultrasoft pseudopotentials [29]. We employ the QUANTUM ESPRESSO software package [30]. A plane wave energy cutoff of 35 Ry and an 8×8 Monkhorst–Pack k-point mesh (per 1×1 in-plane primitive cell) with a Marzari–Vanderbilt smearing of 0.02 Ry [31] are used. A sample 2×1 simulation cell is shown in Figure 1. A typical simulation cell consists of 16 atomic layers of Ge whose bottom layer is passivated with H on top of which 1.5 to 5.5 unit cells (or 3 to 11 monolayers) of BTO are placed. In some cases an electrode is added on top of the BTO. Each cell includes ~ 12 Å of vacuum to separate periodic copies of the system in the z-direction. The in plane lattice constant is fixed to the computed bulk Ge lattice constant of 4.06 Å. All atoms (except the bottom 4 layers of Ge which are fixed to bulk coordinates) are relaxed until the forces on the atoms are less than 10^{-3} Ry/a_0 in all axial directions (a_0 is the Bohr radius). In section III B and section III E we compute the transition energy barrier between different configurations using the nudged elastic bands (NEB) method with climbing images [32].

Because of the asymmetric nature of the simulation cell, the system can have an overall dipole moment which might then interact with the dipole moments of the periodic copies. In other words, because the two surfaces of the slab are in general at different electric potentials, we use the standard dipole correction method [33]: we introduce a fictitious dipole deep in the vacuum region of the simulation cell whose magnitude is self-consistently adjusted so that the entire simulation cell has zero net dipole and thus there are no electric fields deep in the vacuum regions (this corresponds to the physically correct $\vec{D} = 0$ boundary conditions in the vacuum).

III. RESULTS

A. Bulk $BaTiO_3$

$BaTiO_3$ is observed in four structural phases. At high temperature, the cubic perovskite phase is stable. As the temperature is lowered, three structural transitions to ferroelectric phases occur: first to the tetragonal, then to the orthorhombic and lastly to the rhombohedral phase. The microscopic nature of these phases has been the subject of ongoing research. Recently, it has been shown that the phase transitions have both displacive and order-disorder characters [34, 35]. In order to benchmark our computational results against previous studies, we assume a fully displacive model where the ferroelectric phases can be obtained by continuous breaking of symmetry in the cubic phase: the tetragonal, orthorhombic and rhombohedral phases are obtained by breaking the symmetry in the {001}, {101} and {111} directions, respectively, and allowing the atoms and the cells to relax fully. Breaking the symmetry in the {101} direction results in a monoclinic cell with $a = c$, however a twice as large unit cell with higher symmetry (orthorhombic) is used to label this phase. We show the computed energies of each BTO phase in Table I, as well as the experimental temperature range in which each phase is most stable. Our results predict the correct order of phases in the bulk. In Table II, we report the lattice parameters of each phase and compare them to previous theoretical [36] and experimental values [37]. Of course, our first principles simulations using periodic boundary conditions can not describe disordered configurations (which require enormous simulations cells), so these results are not expected to capture all the microsopic details of bulk BTO. Nevertheless, for what follows below, we believe the role of disorder is not critical: the structural distortions in the ultra-thin BTO films on Ge that we study below are dominated by interfacial effects, and the experimentally synthesized BTO films are highly ordered and well-described by first principles theory [1].

Bulk phase	Energy (eV/f.u.)	Temp. (K) [36]
Rhombohedral	$\equiv 0.000$	≤ 180
Orthorhombic	0.002	$180 - 280$
Tetragonal	0.014	$280 - 400$
Cubic	0.068	≥ 400

Table I. Total energies of the structural phases of $BaTiO_3$ at 0 K computed in this work, and temperatures at which each phase is most stable [36].

B. Structure of the $BaTiO_3$/Ge(001) interface

1. *Stoichiometry and periodicity*

Researchers have reported studies of heterostructures involving $BaTiO_3$ and Ge [14, 24, 41] including $BaTiO_3$ thin films directly grown on Ge [25]. However, a study of the direct epitaxial BTO/Ge interface has only recently been published [1]. In this section we present a more detailed account of the *ab initio* investigation of the interfaces discussed in that work.

From a purely theoretical viewpoint, we have enormous

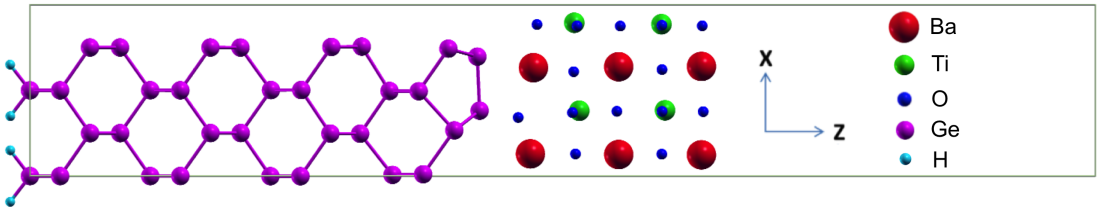

Figure 1. A sample simulation supercell for the BTO/Ge system without a top electrode. The displayed configuration corresponds to the 5 ML thick relaxed BTO, and is in agreement with experiment [1].

Bulk BTO phase	Parameters	This work (Å)	Theoretical ref. [36]	Experimental ref. [37]
Rhombohedral	a, α	4.05, 89.9°	4.00, 89.9°	4.00, 89.8°
Orthorhombic	a, b, c	3.97, 5.77, 5.82	3.98, 5.67, 5.69	3.99, 5.68, 5.69
Tetragonal	a, c	3.99, 4.18	3.99, 4.04	3.99, 4.04
Cubic	a	4.02	3.94	4.00

Table II. Lattice parameters of the bulk phases of $BaTiO_3$ compared with theoretical and experimental references.

Ge surface	E (eV/dimer)	[38, 39]	[40]
flat $p(2\times1)$	$\equiv 0.00$	$\equiv 0.00$	$\equiv 0.00$
buckled $p(2\times1)$	-0.32	-0.24	-0.30
buckled $c(4\times2)$	-0.39	-0.31	-0.38
buckled $p(2\times2)$	-0.40	-0.31	-0.38

Table III. Energies of the four lowest-energy Ge(001) surface reconstructions computed in this work, compared with other theoretical studies.

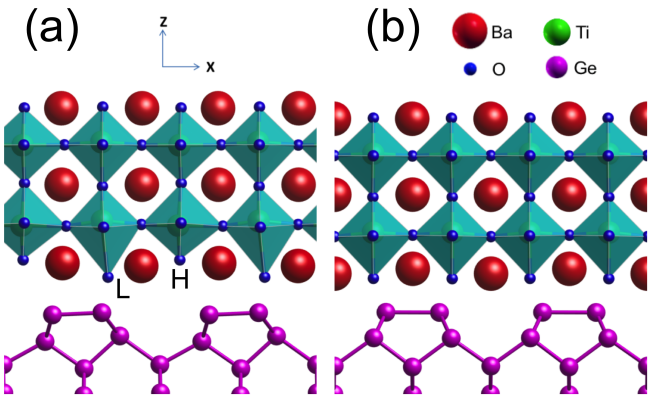

Figure 2. Computed configurations of (a) the ground state (asymmetric) and (b) the metastable state (symmetric) of the 5 ML BTO/Ge interface. The 2×1 unit cell, copied two times in the $x-$direction, is shown for both structures. TiO_6 octahedra are also displayed.

freedom in terms of what type of epitaxial interfaces to explore. First, the atomic layer neighboring the Ge(001) surface, i.e. the interfacial layer, could be BaO or TiO_2. Second, the interfacial layer could be stoichiometric or not. Third, we do not know *a priori* what the in-plane periodicity will be once interfacial reconstructions occur. For the first point, we consult the experimental growth procedure, which starts by depositing 0.5 ML of Ba on the bare Ge surface at 440 °C and another 0.5 ML of Ba at room temperature. This strongly suggests that the interfacial layer is BaO with full barium stoichiometry. We also initially assume full oxygen stoichiometry to begin our analysis (we discuss variable oxygen content in section III E). Finally, we analyze the bare Ge(001) surface in order to decide on the lateral size of the simulation cell.

The Ge(001) surface has been widely studied [38–40] and it is known that the surface atoms strongly prefer to dimerize, which changes the periodicity from 1×1 to 2×1. We find that dimerization lowers the energy by 0.86 eV per dimer. Without changing the periodicity, germanium dimers buckle and lower their energy further by 0.32 eV per dimer. Other reconstructions involve nearby dimers buckling in opposite ways. Some of these further reconstructions lower the energy, which we report in Table III (see the references in the table for detailed descriptions of the surface configurations). Since increasing the periodicity beyond 2×1 does not significantly reduce the energy, we choose to simulate 2×1 cells. We have also checked the validity of this choice *a posteriori* as discussed below.

Structure	Dimer length (Å)	Buckling
Ge(001) $p(2\times1)$	2.5	19.4°
BTO/Ge asymmetric	2.6	2.1°
BTO/Ge symmetric	2.7	0.0°
BTO/Ge no-oxygen	2.9	0.0°

Table IV. Ge dimer length and buckling angle for the bare Ge(001) surface and for the three interface structures studied.

2. *Interface configurations*

We begin by investigating the stoichiometric interface with 5 ML thick BTO (2.5 unit cells), which is one of the two experimentally studied thicknesses [1]. We perform our simulations at the computed Ge lattice constant of 4.06 Å which puts a 1% tensile strain on cubic BTO whose computed lattice constant is 4.02 Å (see Table II). The two lowest-energy structures we have found are shown in Figure 2. We name them "asymmetric" and "symmetric" based on whether they are reflection symmetric with respect to a yz-plane (e.g., a plane cutting through the Ge atoms in the 3rd and 4th Ge layers directly under a dimer). The symmetric structure is found to be 0.39 eV per dimer higher in energy than the asymmetric structure.

The asymmetric interface is chiefly characterized by a large vertical rumpling of consecutive Ba atoms as well as consecutive O atoms in the x-direction. This causes the interfacial TiO_6 octahedra to have different volumes. The octahedra with the lower (higher) interfacial oxygen have a volume of 12.5 $Å^3$ (11.4 $Å^3$). The asymmetric interface also maintains the primary features of the 2×1 Ge(001) surface, i.e. buckled Ge dimers, though the buckling is significantly reduced. See Table IV for a summary of dimer lengths and tiltings. The lower interfacial oxygen (labeled L in the figure) approaches the higher interfacial germanium and makes a bond of length 1.9 Å, whereas the higher interfacial oxygen (labeled H) approaches the titanium above and makes a bond of length 1.8 Å (compare to the 2.0 Å in the high-symmetry cubic bulk BTO). The interfacial oxygens lie in the same xz-planes as Ge dimers and the interfacial bariums lie in the xz-planes that are halfway between consecutive interfacial O-Ge planes (this also holds for the symmetric structure). We have also computed the ground state configuration for the 2×1 slab with no interfacial oxygen, which is analogous to the symmetric oxygenated interface in that it has the same reflection symmetry. Because in this structure the interfacial Ge atoms are neighbors to Ba atoms alone, they accept electrons and therefore dimerize less prominently, as indicated by the elongated Ge-Ge bond length in Table IV.

For the symmetric structure, all the interfacial TiO_6 octahedra have the same volume of 11.6 $Å^3$. They approach the interfacial germaniums and make bonds of length 1.9 Å, whereas their distance from respective titaniums above increase to 2.2 Å. The energy reduction by the formation of the asymmetric (symmetric) interface from the Ge(001) surface and the 5 ML BTO slab in vacuum is 1.18 (0.79) eV per 2×1 cell.

After finding the ground state structure in the 2×1 cell, we have checked whether there are lower energy structures with 2×2 and $c(4\times2)$ periodicities in the following way. We have generated a "reflected" version of the asymmetric interface by reflecting the structure through a yz-plane that leaves the location of the dimer unchanged, but reverses its buckling. This plane leaves the bulk regions of Ge commensurate in the reflected and the unreflected configurations when they are joined in larger simulation cells. Then we have generated 2×2 and $c(4\times2)$ cells by appropriately joining the asymmetric and the reflected asymmetric structures. In both cases we have found that the energy is raised by 0.39 eV per 2×1 cell.

Finally, we have computed the barrier for the uniform transition from the asymmetric to the symmetric structure as 0.57 eV per 2×1 cell, using the NEB method. We demonstrate the results of this computation in Figure 3. Because the transition from the asymmetric structure (labelled "asym - left") to the reflected asymmetric structure (labelled "asym - right") passes through the symmetric structure, the energy landscape has a triple well character: The middle well is higher in energy, the other two wells are symmetry related, and the energy barriers into and out of the middle well are equal to 0.57 eV and 0.22 eV, respectively.

3. *Effects of capping electrode*

We have found in addition that the energy difference between the two physically distinct configurations depends on the choice of the top electrode. We have computed this energy difference for four choices of electrodes: Na, Al, Au and Pt. The results are shown in Table V. We find that as the work function of the electrode increases, the symmetric interface becomes increasingly more favorable compared to the asymmetric interface. We have tested if the trend holds for surface layers that have smaller electron affinity than BaO, such as $BaO_{\frac{1}{2}}$ and Ba. Because of the electron donating oxygen vacancies in these layers, they act as electrodes with low work functions. We show in Table V that the trend holds in both directions: the energy difference between these two configurations can be tuned by the choice of the surface boundary conditions. The underlying reason for this dependence, which is due to preferential electron transfer, is explained in section III C.

In particular, the two polarization states can be made

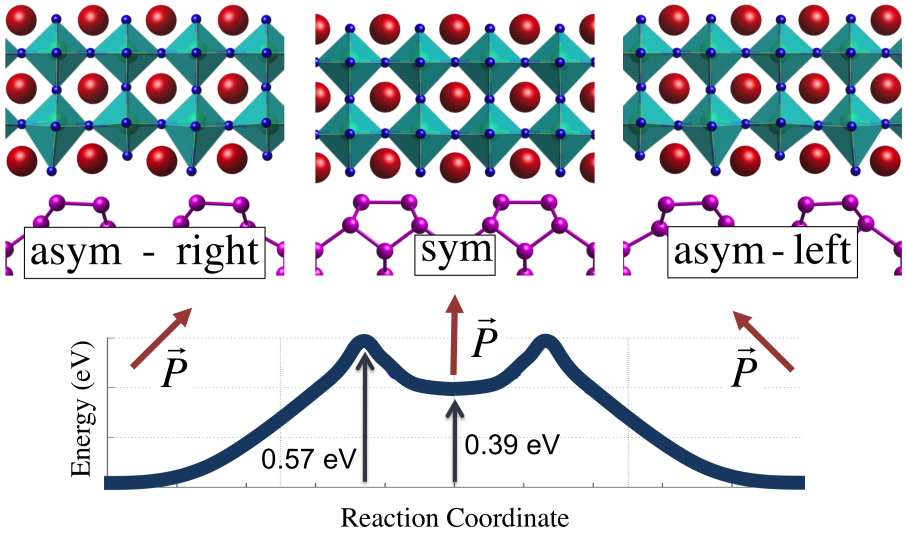

Figure 3. Minimum-energy transition path from the asymmetric structure (labelled "asym - left") to the physically equivalent reflected asymmetric structure (labelled "asym - right"), computed via the NEB method with climbing images. The transition passes through the symmetric structure, which is a local energy minimum. The energy barriers into and out of the symmetric local minimum are 0.57 eV and 0.22 eV, respectively. The polarization direction for each structure is also shown in the figure. The two symmetry related asymmetric structures have opposite in-plane polarizations, but the same out-of-plane polarization.

Top layer or electrode	E(sym) − E(asym) (eV)
Top layer: Ba	0.65
Top layer: $BaO_{\frac{1}{2}}$	0.54
Top layer: BaO	0.39
Na (2.28 eV)	0.44
Al (4.08 eV)	−0.09
Au (5.10 eV)	−0.34
Pt (6.35 eV)	−0.73

Table V. Energy differences between the 5-ML-thick BTO films with the asymmetric and the symmetric interfaces for different top surfaces and electrodes. Oxygen vacancies in the top BaO layer act as electron donors, so an oxygen deficient surface layer acts as an electrode with a low work function. In the bottom four rows the top layer of the oxide is BaO, and the work functions (ϕ) of the electrodes are listed in parentheses [42].

degenerate by the correct choice of the top electrode. In such a situation, when the polarization state is switched by the application of a gate voltage (which is then turned off), there would be no energetic drive to switch back to the other state. Using the four different metal electrodes, we find that the energy difference between the two states depends essentially linearly on the experimental work function of the metal (taken from [42]) and we estimate that an electrode with $\phi = 3.82$ eV would cause the two states to be degenerate in energy.

C. Electronic structure

1. *Interfacial chemistry*

To understand the electronic structure of our interfaces, we first analyze the chemical bonds between the top Ge layer and the interfacial oxide layer. A simple description can be given as follows. For the fully oxygenated interfaces, the primary chemical bonding occurs between the sp^3-like dangling hybrid orbitals of the dimerized Ge atoms (named h_1 and h_2) and the $2p_z$ orbitals of the interfacial O atoms (named p_1 and p_2). For the asymmetric structure (see Figure 4(a), left panel), only h_2 and p_2 overlap to bond. Before the interface has formed, the oxygens are approximately in the O^{2-} state, so p_2 holds two electrons and h_2 holds one electron. After the (h_2p_2) bond has formed, one electron is released and gets accepted by h_1 (see Figure 4(a), middle panel for a level diagram). The $2p_z$ orbital belonging to the other oxygen (namely p_1) does not significantly participate in the process and hence is not shown in the figure. We shall also note that h_1 orbitals weakly mix with the neighboring Ba outer shell orbitals, but not enough to affect the simple description we have given.

For the symmetric interface, on the other hand (see Figure 4(b), left and middle panels), both pairs (h_1, p_1) and (h_2, p_2) bond and two electrons (per 2×1 cell) are released. Due to the lack of available interface states, these electrons are accepted by the Fermi level, and hence the interfacial region becomes doped.

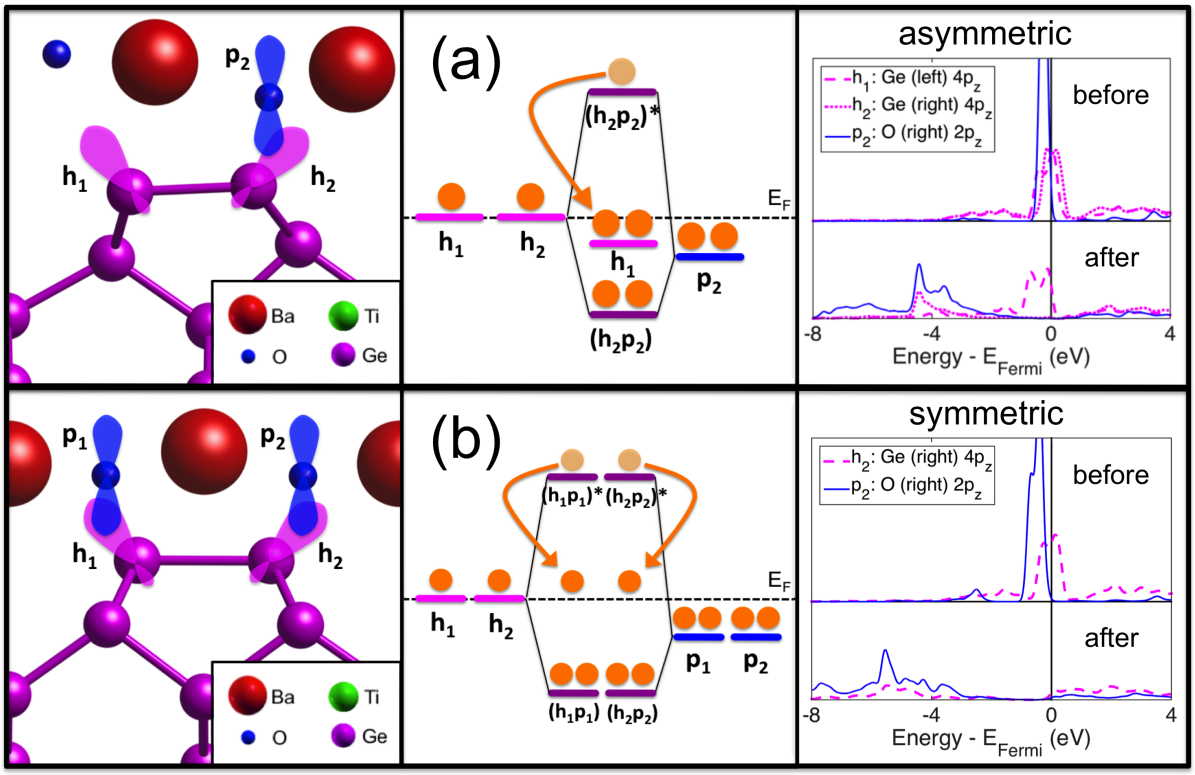

Figure 4. Chemical bonding at (a) the asymmetric and (b) the symmetric interfaces. For each interface configuration, atoms with the orbitals that contribute to the process are shown in the left panel (h_1, h_2 and p_2 for asymmetric; h_1, h_2, p_1 and p_2 for symmetric—see text for details); a level diagram that describes the electron occupations of atomic states both before and after the formation of the bonds is shown in the middle panel; and densities of states projected onto the participating orbitals (PDOS) both before and after the formation of the interface are shown in the right panel (Only one pair of orbitals, i.e. h_2 and p_2, is shown for the symmetric interface because of the equivalence of the other pair due to the symmetry of this structure). The zero of energy is taken as the Fermi level and is shown as a solid vertical line.

In order to further demonstrate the bonding, we show the relevant projected densities of states (PDOS) for both interfaces before and after interface formation in the right panels of Figure 4. We use Ge $4p_z$ orbitals to represent the dangling orbitals h_1 and h_2 because we expect them to closely align with the $z-$axis due to the dimerization of the interfacial Ge atoms. We have verified this by plotting all PDOS and observing that $4p_z$ orbitals are the only Ge orbitals that are relatively sharp and centered at the Fermi level. For the asymmetric interface we observe that h_2 (initially half-occupied) and p_2 (initially fully occupied) interact to create a bonding state at low energy, whereas the initially half-filled h_2 becomes mostly filled. For the symmetric interface we only display one pair of orbitals, i.e. h_2 and p_2, because the two pairs are equivalent by symmetry. The fully occupied p_2 and the half-occupied h_2 interact to create a bonding state at low energy which is filled, and the conduction band edge is pushed below the Fermi level to accommodate the donated electrons.

This picture of the interfacial chemistry is corroborated by the fact that electrodes with higher electron affinity lower the energy of the symmetric interface with respect to the asymmetric interface (see Table V). We find that more electrons are transferred to the electrode in the symmetric case compared to the asymmetric, since there are more mobile electrons in the former. The difference in the transfer of charge is visible in Figure 5, where the spatial electronic density redistribution is plotted for (a) the asymmetric and (b) the symmetric interfaces. For each structure, we have computed the electron density of the full Au/BTO/Ge system, $n_{\mathrm{Au/BTO/Ge}}(x,y,z)$, and the isolated Au and BTO/Ge systems with the same atomic positions as the full system, $n_{\mathrm{Au}}(x,y,z)$ and $n_{\mathrm{BTO/Ge}}(x,y,z)$. We have then computed the difference in the density due to the addition of the elec-

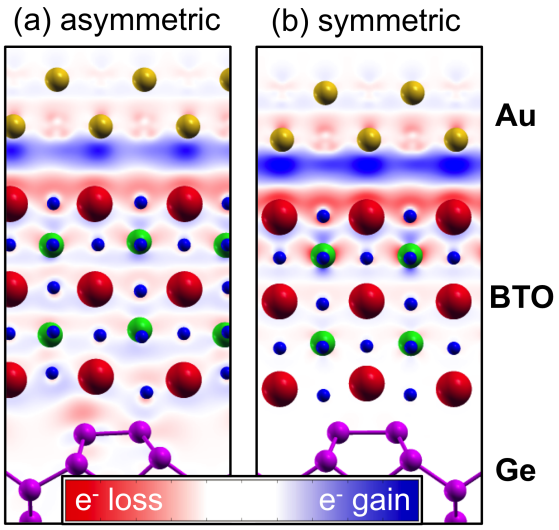

Figure 5. Electron density redistribution due to the addition of a Au capping electrode for (a) the asymmetric and (b) the symmetric structures. The plotting is done in the xz-plane by averaging the redistribution in the y-direction.

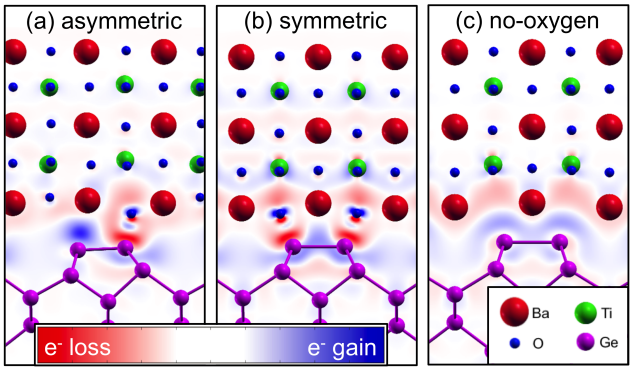

Figure 6. Electron density redistribution for (a) the asymmetric, (b) the symmetric and (c) the oxygen-free interfaces. The plotting is done in the xz-plane by averaging the redistribution in the y-direction.

trode: $\Delta n\,(x,y,z) = n_{\mathrm{Au/BTO/Ge}}\,(x,y,z) - n_{\mathrm{Au}}\,(x,y,z) - n_{\mathrm{BTO/Ge}}\,(x,y,z)$. After averaging the values in the $1\times$ direction, the resulting $\overline{\Delta n}\,(x,z)$ is shown in Figure 5. We have also computed the total charge transferred to the electrode to be 0.24 (0.29) e^- per 2×1 u.c. for the asymmetric (symmetric) structure. This allows the symmetric interface to have fewer electrons in the high energy conduction band states when an electrode is present. Using an electrode with a higher work function allows more of the mobile electrons to migrate, further lowering the energy of this structure. Conversely, oxygen vacancies in the BTO surface layer donates electrons into the system, further doping the conduction band in the symmetric case and increasing its energy.

For the oxygen-free interface, we have checked that prior to the interface formation the interfacial barium is approximately in the Ba^0 state using the PDOS data for Ba orbitals. The interaction between the interfacial Ge and Ba chiefly consists of ionic electron transfer from Ba to Ge, with a weak covalent mixing between the Ge dangling orbitals and Ba outer shell orbitals. Since there are four Ba valence electrons (per 2×1 cell) but room for only two electrons in the Ge dangling orbitals, two electrons are donated to the Fermi level, as occurs in the case of the symmetric interface. Because the same number of electrons are accommodated by the conduction band which consists of similar states in the two interfaces, the band alignments and the polarization profiles of these two interfaces are highly similar, as we shall present below.

2. *Electron redistribution due to interface formation*

To further illustrate the electronics of the interface, we have computed the spatial electronic density redistribution for all three interfaces as $\Delta n\,(x,y,z) = n_{\mathrm{BTO/Ge}}\,(x,y,z) - n_{\mathrm{BTO}}\,(x,y,z) - n_{\mathrm{Ge}}\,(x,y,z)$. After averaging the values in the $1\times$ direction, we show the resulting $\overline{\Delta n}\,(x,z)$ is in Figure 6. A few comments can be made by inspecting the plots: (i) The most significant electronic redistribution occurs along Ge-O bonds; (ii) In the asymmetric structure, the Ge atom which does not neighbor an O accepts electrons; but the spatial region accepting region points to the neighboring Ba which is expected due to the positive formal charge state Ba^{2+}; and (iii) For both the symmetric and the no-oxygen cases, the interfacial Ba(O) layer loses some electrons to the neighboring Ge and TiO_2 layers.

3. *Band alignments*

We have found that the two different types of the stoichiometric BTO/Ge interface contains different chemical bonds and give rise to differences in electronic structure. In order to predict the electrical properties of this system for potential device applications, we now turn to a study of the alignments of energy levels. Our above analysis of the interfacial chemistry suggests that the position of the Fermi level is pinned by the interface in both cases. However, in order to infer the spatial behavior of the electronic energy levels throughout the system, we need to express the states in terms of localized functions in real space, such as projections onto atomic orbitals.

We determine the band alignments using a threshold

method based on an examination of the layer-by-layer DOS of the semiconductor-oxide system. See Figure 7 for examples of the application of the threshold method. For each atomic layer, we sum the DOS projected onto all the atomic orbitals that belong to that layer and plot with a Gaussian broadening. We then find the energy values for each layer where the DOS of the layer is at a threshold to determine the layer by layer band edges throughout the system. We finally decide which layers are sufficiently bulk-like and report the band edges based on those layers. The threshold method as explained is sufficient for a qualitative description of the band alignment. However, the choice of the threshold requires careful analyses of the bulk band structure and DOS so that it reproduces the band edges in the bulk. In addition, due to the well known problem of underestimation of band gaps in density functional theory, we have modified the band edges in order to correct the gaps to match their experimental values in the two materials. For complete details of the determination of band alignments, see section §V.

The main difference in the band alignments of the asymmetric and the symmetric interfaces is the nature of the interfacial states. For the asymmetric system, the interfacial region is dominated by the mostly filled dangling orbital of one of the germaniums (labelled h_1 above) around the Fermi level. These electronic states decay slowly into the Ge due to its small band gap. The weak covalent mixing between h_1 and the nearby Ba outer shell orbitals is manifest as a nonzero DOS for the interfacial BaO layer within the band gap of $BaTiO_3$. For these reasons, in the vicinity of the interface the projected densities of states are not bulk-like and the band edges are not well defined. We instead schematically display the approximate extent of the interface states as rectangles (see Figure 8 (a) and (c)). Figure Figure 7 (a) shows the layer-by-layer PDOS for the asymmetric interface system detailing these points.

For the symmetric system, the PDOS curves in the vicinity of the interface show sufficient bulk-like character to allow us to trace the band edges all the way to the interface. In Figure 7 (b) we show the band bending near the symmetric interface as dashed curves as well as the band edges computed from the bulk-like regions of Ge and BTO as dashed lines. The ejection of electrons from the interfacial region causes the symmetric structure to be electron doped in the vicinity of the interface (see Figure 8 (b) and (d)).

For both structures, the effect of a top electrode (in our case Au) is similar: it accepts mobile electrons from the interfacial system and hence moves the bands upward with respect to the Fermi level. For the asymmetric structure, the effect is more striking because the valence band of the oxide is moved all the way up to the Fermi level. This is because the asymmetric interface has fewer available states in the oxide near the Fermi energy. See Figure 9 for plots of local densities of states (LDOS) at

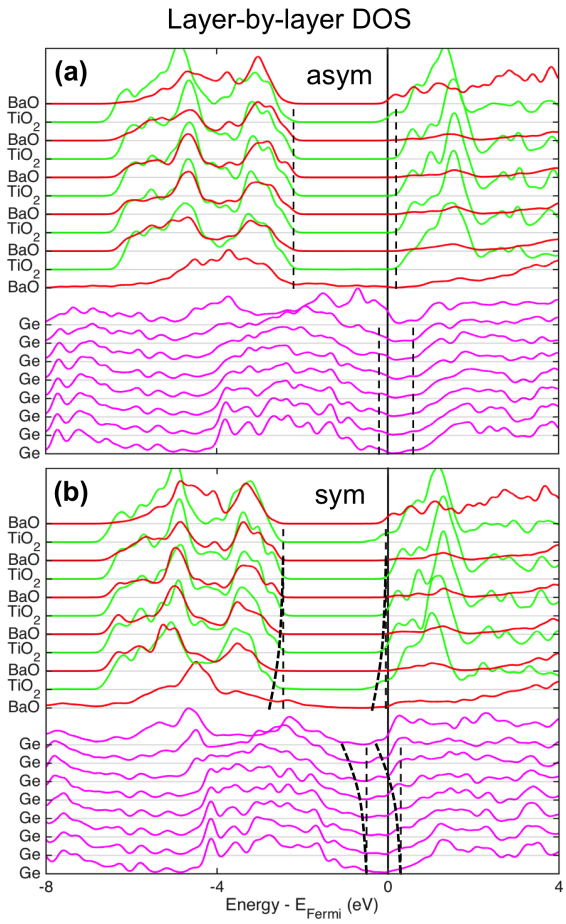

Figure 7. Layer-by-layer DOS for (a) the asymmetric interface and (b) the symmetric interface without a top electrode. The zero of energy is taken as the Fermi energy of the system. The valence and the conduction band edges deep inside either material in both sides of the interface are shown as vertical dashed lines. The curved dashed lines trace the layer dependent band edges as determined by our threshold method (see text and section §V for complete details). Only 8 of the 16 Ge layers are shown in the figure.

the Fermi level for the asymmetric and symmetric interfaces. For the asymmetric interface, the LDOS at E_{Fermi} is mostly dominated by the dangling orbital of the interfacial Ge, there is some density near the top surface of the BTO, and the interior of the BTO is essentially insulating. In contrast, for the symmetric interface, the LDOS at E_{Fermi} is nonzero throughout the interface region and inside the oxide. Therefore, for the asymmetric interface, there are fewer mobile electrons available for transfer to the electrode, which permits the valence band edge to move all the way up to the Fermi level in the oxide to accommodate this charge transfer.

Because of the charge transfer to the electrode, an electron potential is created which increases from the interface to the electrode. This potential in turn enhances the out-of-plane ionic polarization of the film, which creates

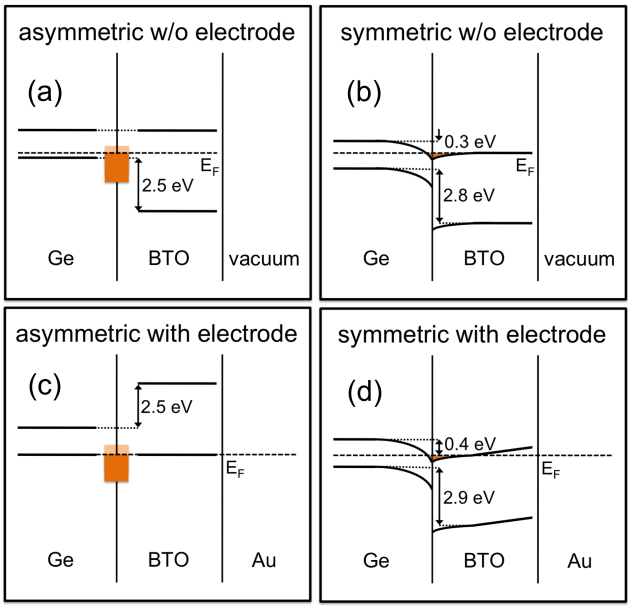

Figure 8. Band alignments for the asymmetric and the symmetric interfaces, with and without a gold electrode. The orange shaded rectangles in the alignments of the asymmetric structure represent interface states that extend into both materials and are partially filled. The orange shaded regions in the alignments of the symmetric structure represent the electron doping around the interface. The alignment for the no-oxygen interface is the same as for the symmetric interface.

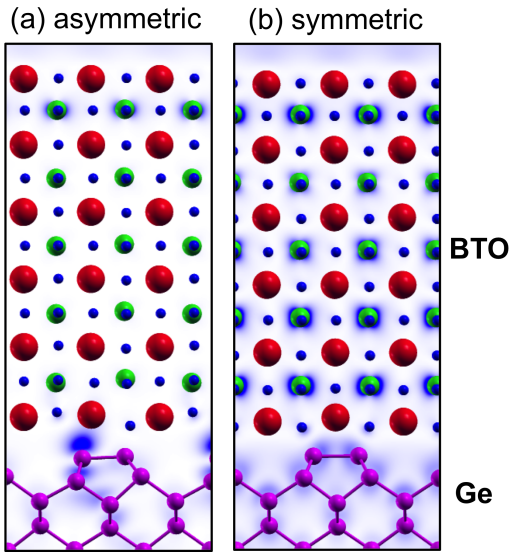

Figure 9. Local densities of state (LDOS) at the Fermi level for (a) the asymmetric and (b) the symmetric structures for the 5.5 u.c. thick $BaTiO_3$ on Ge. The plotting is done in the xz-plane by averaging the LDOS in the y-direction.

a potential for electrons that decreases from the interface to the electrode. For the asymmetric structure these two competing effects on the potential are in balance and thus the band edges in the oxide region are flat. For the symmetric structure, however, the electron transfer to the electrode is more significant than the enhancement of the ionic polarization; therefore the band edges in BTO have an upward slope going from Ge to Au. The experimental studies on the BTO/Ge heterostructures have reported the conduction band edges to be approximately aligned [24, 25], which suggests that the interfacial chemistry in these experimental systems is similar to the symmetric interface.

We observe that band edges in Ge are positioned differently in the two polarization states, suggesting carrier density modulation in the semiconductor, i.e. the conducting properties of the Ge substrate are affected by the thin film oxide. A similar field effect has been observed in BTO/STO/Ge heterostructures [14]. We further observe that the asymmetric and the symmetric structures have alignments that promote different charge carriers through the system: asymmetric favors holes, and symmetric favors electrons. Since these two configurations can be made approximately degenerate by the choice of the top electrode, it may be possible to switch between these phases with an electric field, as discussed in section III B. Because of the different charge carriers in the two phases, switching between them would change the polarization state as well as the dominant carriers for charge transport. To our knowledge this phenomenon of ferroelectricity combined with carrier type switching has not been observed before and may be useful in potential device applications.

Before we end this section, we note that the existence of polar distortions and their possible switchability in the presence of mobile charge carriers is unexpected. For a thick film, mobile carriers in the film would screen external electric fields and prevent polarization switching. However, the screening length of carriers is always finite, and if it is large enough, the portions of the film inside the screening length will feel an imposed field. And we find that the screening length in our ultra-thin BTO films are long enough for this to be a plausible switching mechanism. For example, the symmetric interface has a high carrier density, but as Figure 7(b) shows, even in this case the screening length is larger than a unit cell (i.e, the "bowing" of the band edges in going from Ge to BTO extends over multiple atomic layers). Separately, using a generalized Thomas–Fermi model, we estimate the screening length to be ~ 7Å or higher, which means that a substantial part of BTO film resides within the screening region and can respond to an external electric field [43]. (See section §V for the details of the screening length estimation.)

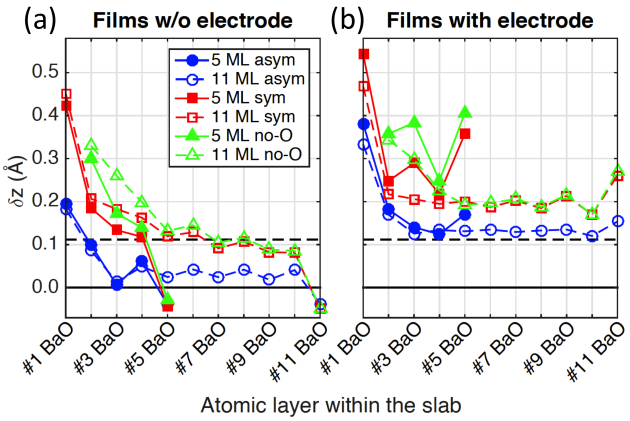

Figure 10. Layer-by-layer polarization profile as measured by cation-anion vertical displacement (δz) for 5 ML and 11 ML thick BTO films, plotted for the asymmetric, symmetric and oxygen-free interfaces. The profiles are displayed for the cases where the films (a) are not capped with an electrode and (b) are capped with 2 ML of Au. The #1 BaO layer is the interfacial oxide layer. The dashed horizontal lines show the computed value of δz for orthorhombic bulk BTO, strained in the xy-plane to Ge lattice parameters.

D. Film polarization

1. *Polarization profile*

The chief difference between the asymmetric and the symmetric interfaces in terms of ionic polarization is that the asymmetric interface is polarized along $\pm x$- and z-directions, whereas the symmetric interface is polarized only along the z-direction. In order to characterize the out-of-plane polarization, we introduce the parameter δz as the average cation-anion displacement in a given layer, i.e. $\delta z = \overline{z\,(\text{cation})} - \overline{z\,(\text{oxygen})}$. We have calculated δz for each atomic layer of the BTO film for the asymmetric, symmetric and no-oxygen interfaces for various thicknesses. We have also introduced a capping electrode (2 monolayers of gold) in order to investigate the effect of boundary conditions.

We present our findings in Figure 10 for the 5 ML and 11 ML thick films, which are the two cases studied in the experiment [1]. When the film is not capped with an electrode (see Figure 10 (a)), we find that the top BTO layer pins the surface polarization to the same value for all interfaces, which causes a sudden drop in the polarization profile from the interface to the surface for the thinner films. For the thicker films, polarization reduces for the first two unit cells and remains approximately constant up to the surface. The symmetric configuration (labelled "sym") has a significantly higher polarization than the asymmetric configuration (labelled "asym") throughout the film. The structure with no interfacial oxygen (labelled "no-O") has a similar profile to the oxygenated symmetric structure. The positive interfacial polarization, which is common in all interfaces, is best understood as follows: In all three interfaces there is a transfer of electrons from the interfacial region to the oxide. The resulting electronic dipole pushes the positive (negative) ions up (down), pinning the interfacial δz. In the absence of a well screening electrode, the depolarizing field causes the polarization to decay quickly. In "sym" and "no-O" because of the doping of the conduction band, there are mobile charges in the oxide which screen the depolarizing field so that the polarization in the interior is non-zero. These findings are quite similar to the findings of the previous work on the $SrTiO_3$/Si system, where presence of mobile charges determine the value of the layer polarization away from the interface [44].

When the film is capped with a gold electrode (see Figure 10 (b)), the top BaO layer bucklings are no longer pinned and have different values for different thicknesses and interfacial configurations. We observe also that with a gold electrode polarization increases throughout the film for all structures. This is because Au has a large work function and thus attracts electrons from the Ge/BTO system, which in turn enhances the ionic polarization toward the electrode, as we have discussed above. We also observe that "sym" and "no-O" interfaces have very similar profiles that are more polarized than "asym". This is because of the combined effect of more mobile charges in the oxide and more electron transfer to the electrode in these structures compared to "asym". We finally observe in Figure 10 (b) that δz is generally higher in thinner films than thicker films in a given oxide layer. This is because in thinner films there are fewer oxide states to accommodate the electrons donated from the interface, causing more of the electrons to go to the electrode, and thereby creating a larger electric field.

2. *Effects of film thickness*

In addition to the 5 ML and the 11 ML thick films studied experimentally [1], we examine the ionic polarizations of films ranging in thickness from 3 to 11 monolayers. We summarize the results in Figure 11. We first observe that for all films with and without a capping electrode, the average polarization has a small modulation due to the surface termination of the oxide. For films without a capping electrode, the average δz has almost no thickness dependence. This is explained as follows: the higher values of δz are confined to the first few layers of the film, lowering the average polarization as the thickness increases. However, because the decay of the polarization becomes more gentle as the thickness increases, especially for "sym" and "no-O", this effect is mostly cancelled. For the films with a gold electrode, both because the profile is flat after the

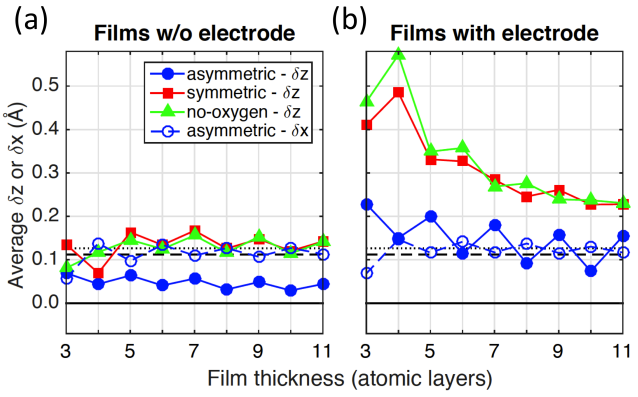

Figure 11. Average film polarization as measured by cation-anion vertical displacement (δz) for BTO films with different thicknesses, plotted for the asymmetric, symmetric and oxygen-free interfaces. The in-plane polarization of the asymmetric film is also displayed as measured by the parameter δx (described in text). The results are displayed for the cases where the films (a) are not capped with an electrode and (b) are capped with 2 ML of Au. The dashed (dotted) horizontal lines show the computed value of δz (δx) for orthorhombic bulk BTO, strained in the xy-plane to Ge lattice parameters.

vicinity of the interface and because the near-interface δz is higher for thinner films, the decrease of the average δz with thickness is more significant. This finding is in agreement with the previously studied $SrTiO_3$/Si system, where for well screened films the average polarization decreases with film thickness [44]. Finally we observe that the in-plane polarization that is present in the asymmetric film, i.e. δx is mostly unaffected by thickness and the presence of a capping electrode. The in-plane polarization, δx, is defined as the horizontal displacement of ions in an atomic $yz-$plane, averaged through all four inequivalent such planes in the 2×1 cells.

E. Oxygen content

1. *Energetics of oxygen vacancies*

In order to understand the oxygen content of the films, we have computed the formation energies of oxygen vacancies. First, we have relaxed both the asymmetric and the symmetric structures with one oxygen atom omitted per 2×1 cell. We have repeated this for each unique oxygen site. We have found that in both the asymmetric and symmetric structures, the smallest formation energy for an oxygen vacancy takes place when the vacancy is in the interfacial BaO layer. In Table VI we summarize the formation energies of O vacancies vs layer in both structures. Formation energies are computed as the energy cost of removing an oxygen from its position in the film and placing it into an O_2 molecule in vacuum.

Structure	#1 B	#2 T	#3 B	#4 T	#5 B
asym (a)	3.7	5.2	4.7	5.3	5.1
asym (b)	3.7	5.2	4.7	5.2	4.5
asym (c)	3.7	4.1	4.8	5.4	5.0
sym (a)	3.6	5.6	5.0	5.5	5.5

Table VI. Formation energies of O vacancies (eV per vacancy) for the asymmetric and symmetric structures, vs atomic layer. For each atomic layer, the lowest formation energy among possible vacancies is shown. BaO layers are labelled with "B" and TiO_2 layers are labelled with "T". The layer labelled as #1 (#5) B is the BaO layer at the interface (surface). (a) 1 vacancy per 2×1 cell; (b) 2 vacancies per 2×2 cell; (c) 1 vacancy per 2×2 cell.

For the asymmetric structure, in addition to relaxing the structures with 1 vacancy per 2×1 cell, we have relaxed structures with 2 vacancies per 2×2 cell, where the vacancies are close enough to be considered neighbors. We list in Table VI vacancy formation energies where the 2 vacancies in the 2×2 cell are in the same atomic layer (only the average energy of the 2 vacancies is shown for each layer). Formation energies of vacancies which reside in different atomic layers in these 2×2 cells are not significantly different, and are omitted to simplify the discussion. Finally, to compare these results with a different vacancy density, we list the formation energies of structures with 1 vacancy per 2×2 cell for the asymmetric structure. We find that the interface is the most energetically favored place for a vacancy for this case as well, indicating that this conclusion holds for the isolated vacancy limit.

Our finding that the interface is the least costly location for an oxygen vacancy irrespective of vacancy density and configuration is in agreement with the previous work on the $SrTiO_3$/Si system [45]. In that work it is argued that this is due to the chemical differences between the interfacial region and the interior of the oxide film. An oxygen vacancy can be thought to donate two electrons to the available states nearby. For a vacancy at the interface, there are low-energy Si dangling bond states that accept the donated electrons. However, for a vacancy in an interior layer of the oxide, it is found that high energy conduction band states with Ti $3d$ character get filled by the donated electrons [45]. Because Ge is isovalent with Si, we expect these findings for the $SrTiO_3$/Si system to apply to the $BaTiO_3$/Ge system as well.

2. *Thermodynamics of oxygen content*

Having established that oxygen vacancies favor the interfacial BaO layer, we investigate the thermodynamics of interfacial oxygen vacancies. We have computed

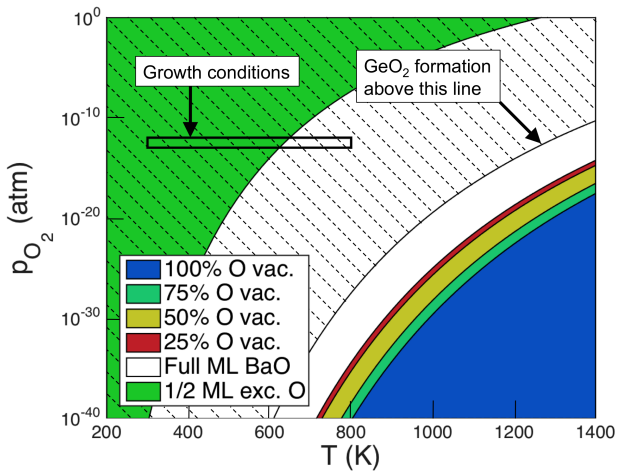

Figure 12. Computational phase diagram for oxygen stoichiometry in a BTO thin film grown on Ge(001). Larger and larger vacancy concentrations are thermodynamically favored as one moves to the lower right corner of the diagram. An interface with excess oxygen is preferred at the upper left corner. The vacancies or excess oxygens lie in the interfacial BaO_x layer, which is found to be the most favorable location for a given stoichiometry. The experimental growth conditions described in [1] are shown as a rectangular region, and the region unstable to GeO_2 formation is shaded.

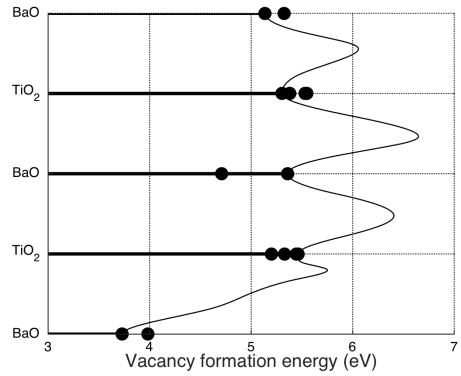

Figure 13. Vacancy formation energies for each unique site in the 5 atomic layer BTO film are shown layer by layer as solid circles. The bottom of the plot corresponds to the interface. A set of transition minimum energy paths that are computed via the NEB method are also shown as a solid curve going through a vacancy site in each layer.

the lowest energies for the interfaces with varying interfacial vacancy densities, using 2×1, 2×2 and 4×1 cells, and calculated the vacancy formation energies vs density. In order to build a phase diagram, we simply assert that a vacancy density is thermodynamically favored at temperature T and oxygen partial pressure p_{O_2} if $\mu_O(T, p_{O_2}) + E_{\text{formation}} < 0$. We then use the expression [45]

$$\mu_O(T, p_{O_2}) = \frac{1}{2} g_{O_2}(T) + \frac{1}{2} k_B T \ln\left(\frac{p_{O_2}}{1\text{atm}}\right), \quad (1)$$

where $g_{O_2}(T)$ is the Gibbs free energy of O_2 in gas phase at temperature T and $p_{O_2} = 1$atm. We use the experimental measurements for $g_{O_2}(T)$ [46] in order to create the phase diagram shown in Figure 12. We also show the growth conditions as a rectangular region where $300\text{K} < T < 800\text{K}$, $10^{-13}\text{atm} < p_{O_2} < 10^{-12}\text{atm}$. The details of the growth are presented in Ref. [1]. The phase diagram indicates that during the growth, vacancies are not thermodynamically stable. We have also computed the energies of the structures where the interface has 0.5 ML of excess oxygen. The region where excess interfacial oxygen is thermodynamically more stable is shown on the phase diagram, and it partially coincides with the growth conditions.

Lastly, for a comprehensive understanding of the oxygen content in the film, we have calculated the oxygen chemical potential at which bulk crystalline GeO_2 becomes as stable as bulk crystalline Ge and O_2 gas, as they exist separately. GeO_2 becomes more stable if $\mu_O(T, p_{O_2}) > \frac{1}{2}(E_{GeO_2} - E_{Ge} - E_{O_2})$, which holds for the shaded area in Figure 12, which covers the entire region corresponding to the growth. This well-known vulnerability of the Ge surface to oxygenation is experimentally overcome by kinetic trapping.

3. *Kinetic trapping of oxygen*

In order to gain theoretical insight about GeO_2 prevention as well as oxygen stoichiometry, we have performed NEB simulations for oxygen vacancy migration within the film, as shown in Figure 13. For the 5 ML asymmetric BTO, there are 14 distinct oxygen sites, each of which yields a unique relaxed structure when vacated. Figure 13 presents their vacancy formation energies as well as a set of representative minimum energy transition paths for inter-layer vacancy migration. We find that, in addition to the fact that a vacancy costs over an electron-volt more energy when it is not at the interfacial BaO layer, there are energy barriers of ~ 1 eV for vacancy migration between non-interfacial BTO layers. This indicates that once the initial few layers of BTO are deposited, the vacancies formed at the interface are kinetically trapped at the interface.

Let us consider the following process for increasing the oxygen content of the interface beyond stoichiometry: An O atom at the interfacial BaO layer breaks from the film and binds directly to the Ge surface. We have found the minimum of the energies of such configurations to be 1.9 eV higher than the stoichiometric asymmetric film, which causes this event to be unlikely. Once this occurs, a newly formed interfacial vacancy should migrate up into the film and reach the top BaO layer, which is

both energetically and kinetically inhibited. Lastly the surface oxygen vacancy should be filled by atmospheric O_2, completing the process which in effect adds an extra oxygen to the interface. Therefore in spite of the fact that interfaces with excess oxygen, and eventually full oxygenation of the germanium surface, are thermodynamically favored for this film, once the initial few layers of BTO are deposited, the oxygen content remains stable. This mechanism for trapping the oxygen in the oxide film rather than oxygenating the substrate is similar to the proposed mechanism for $SrTiO_3$/Si [45].

IV. CONCLUSION

We have conducted an *ab initio* study of the epitaxial $BaTiO_3$/Ge interface which has potential technological applications. We have found that ultrathin films of BTO grown on Ge(001) surface with full oxygen stoichiometry can occur in two 2×1 configurations with different ionic polarizations. This is in contrast to the similar $SrTiO_3$/Si system, where a 1×1 configuration is observed and the interface polarization is predicted to be fixed [18]. With a capping electrode that has the appropriate work function, the two polarization states of BTO films on Ge can be made degenerate, enabling a potentially robust ferroelectric thin film oxide. We have analyzed the interface chemistries and the resulting electronic structures in the two polarization states. We have shown that the band alignments for these phases prove that there is significant carrier density modulation in the semiconductor, to the degree of changing the dominant carriers in the intrinsic semiconductor limit. Ferroelectric switching coupled with carrier type switching may have novel uses in device applications. We have examined the ionic polarization profile of these films for a range of thicknesses. We have found that the differences in interfacial chemistry lead to differences in polarization profile, as in the previously studied STO/Si case [44]. We have finally discussed the oxygen content of the ultrathin oxide by a detailed analysis of energetics of oxygen vacancies in the film. We have found that the thermodynamic tendency for the oxygenation of the Ge surface is kinetically inhibited, and once a few atomic layers of BTO are deposited, the oxygen stoichiometry becomes stable. This mechanism of kinetic trapping is similar to the mechanism that stabilizes the STO/Si interface [45].

V. APPENDIX A: BAND ALIGNMENT DETERMINATION

We determine the band edges in the two materials based on an analysis of layer-by-layer projected densities of states. We first plot all layer-by-layer DOS for a given configuration as in Figure 7. Then, for the layers whose DOS are bulk-like, we find where the DOS falls below a certain threshold around the Fermi level. We choose the threshold for each side of the interface based on the DOS of bulk Ge and bulk BTO, where we know the exact band structures and the band gaps. However, due to the well known DFT underestimation of band gaps, we obtain a bulk BTO with a gap of 1.7 eV compared to 3.2 eV measured experimentally [47]. Moreover, the bulk Ge we compute has no gap while the experimental gap is 0.7 eV [48].

A standard way to overcome this shortcoming of DFT is by applying a Hubbard U correction to atomic orbitals that comprise either the valence or the conduction band edge [49]. This method, commonly known as DFT+U, effectively decreases (increases) the energy of a DFT eigenstate, which overlaps with the chosen atomic orbital, if it is more (less) than half occupied. If the eigenstates that overlap with the chosen orbital comprise the VBE and/or CBE, this procedure increases the band gap. In addition to correcting the gaps, DFT+U simulations of the BTO/Ge system allow us to ascertain how the Fermi level is pinned and how the band edges in BTO and Ge relatively align as the gap in either material is varied. We have run simulations with Hubbard U applied to Ti $3d$ states and/or Ge $4p$ states. We present a representative set of results from these simulations in Table VII.

By close examination of the layer-by-layer DOS of each such simulation and application of the threshold method, we identify the band edges and how they depend on the applied U. For (a) the asymmetric interface without electrode, we observe that the Fermi level is pinned by the interfacial states, and the gap in either material changes with U by moving the VBE down and the CBE up by similar amounts. We conclude that for this case the midpoint of the gap in both materials is approximately fixed with respect to U and adjust the band edges accordingly. For (b) the asymmetric interface with electrode, we find that the Fermi level is pinned by the interfacial states, and that the VBE of BTO is fixed at the Fermi level. For the symmetric interface (c) without the electrode and (d) with the electrode, we find that the Fermi level is pinned at the CBE in both materials.

As a final step in determining the band edges, we have tested the accuracy of the threshold method in bulk BTO and Ge. We have run DFT+U simulations on the bulk materials where the Hubbard U is applied to Ti $3d$ states and Ge $4p$ states, with $U = 0, 1, 2, \ldots, 9$ eV. We summarize the results in Figure 14.

For (a) BTO the band gap is determined by the highest occupied state at the R point, and the lowest unoccupied state at the Γ point in the Brillouin zone. For very high values of U, we find that the order of lowest occupied bands switch and the gap starts to decline. Therefore DFT+U is unable to reproduce the experimental band gap of 3.2 eV. However, we find that it is possible to choose the threshold such that the band edges from the

Hubbard U (eV)	(a) BE in asym w/o Au	(b) asym with Au	(c) sym w/o Au	(d) sym with Au
$U_{\rm Ge}=0$, $U_{\rm BTO}=0$	Ge: −0.2, 0.6 BTO: −2.2, 0.2	−0.1, 0.7 0.0, 2.4	−0.5, 0.3 −2.4, 0.0	−0.4, 0.4 −2.4, 0.0
$U_{\rm Ge}=3$, $U_{\rm BTO}=0$	Ge: −0.3, 0.7 BTO: −2.1, 0.3	−0.2, 0.8 0.0, 2.4	−0.7, 0.3 −2.4, 0.0	−0.6, 0.4 −2.4, 0.0
$U_{\rm Ge}=3$, $U_{\rm BTO}=3$	Ge: −0.3, 0.7 BTO: −2.2, 0.4	−0.2, 0.8 0.0, 2.6	−0.7, 0.3 −2.6, 0.0	−0.6, 0.4 −2.6, 0.0
Summary:	Midpoint of gap approx. fixed in Ge and BTO.	Midpoint of gap fixed in Ge, VBE at $E_{\rm Fermi}$ in BTO.	CBE at $E_{\rm Fermi}$ in Ge and BTO.	CBE at $E_{\rm Fermi}$ in Ge and BTO.
Final band edges:	Ge: −0.1, 0.6 BTO: −2.6, 0.6	0.0, 0.7 0.0, 3.2	−0.4, 0.3 −3.2, 0.0	−0.3, 0.4 −3.2, 0.0

Table VII. Band edges (BE) in the oxide and the semiconductor for the asymmetric and the symmetric interfaces, with and without the capping electrode, determined by the threshold method, for three sets of Hubbard U parameters. For a given configuration and a set of Hubbard U, the four numbers are VBE(Ge), CBE(Ge), VBE(BTO) and CBE(BTO), respectively. In each case the zero of energy is taken as the Fermi level and the units are electron-volts. See the text for further explanation of the determination of the final band edges. The no-oxygen interface has identical alignments as the symmetric interface.

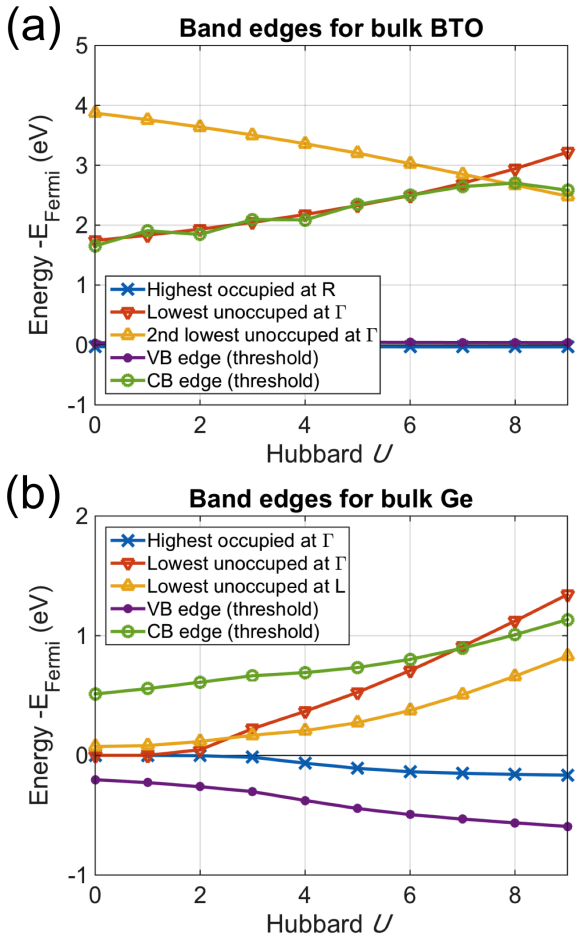

Figure 14. Bulk band edges of (a) BTO and (b) Ge vs a Hubbard U applied to Ti $3d$ states and Ge $4p$ states, respectively (see text for the description of the curves).

threshold method are indistinguishable from the band edges we obtain directly from the band structure. Therefore in the thin film simulations we take the band edges from the threshold method to be correct and rigidly shift them to set the gap to the experimental value.

For (b) Ge the band gap is determined by the highest occupied state at the Γ point, and the lowest unoccupied state at the L point in the Brillouin zone. However we find that for $U = 0, 1, 2$ eV the lowest unoccupied state at Γ is practically degenerate with the highest occupied state at Γ, and hence the gap vanishes. For higher values of U the gap monotonically increases as expected. We find that the threshold value that reproduces the band gap for higher U is too low to predict the band edges for lower U, because the DOS does not fall below the threshold around the Fermi level. Hence we choose a threshold which overestimates the band gap for a given U but reproduces the shapes of the VBE vs U and CBE vs U curves as closely as possible. We find that the experimental band gap is reproduced in the band structure for $U \simeq 7$, with VBE $= -0.1$ and CBE $= 0.6$. For $U = 0$ the threshold method yields VBE $= -0.2$ and CBE $= 0.6$. So in order to estimate the band edges in the film, after analyzing the Fermi level pinning and relative movement of the edges with respect to changing gaps, we determine the final positions of the Ge band edges for $U = 0$ case, and shift VBE up by 0.1 eV. Therefore we finally arrive at the band edges listed in Table VII and displayed in Figure 8.

VI. APPENDIX B: SCREENING LENGTH ESTIMATION

In order to estimate a lower bound for the screening length of thin films of $BaTiO_3$, we begin with the Pois-

son's equation in CGS units:

$$\nabla^2\phi = -4\pi\rho, \tag{2}$$

where ϕ is the electrostatic potential and ρ is charge density. ρ can be written as a sum of the charge densities due to mobile carriers, bound charges (ions and electrons in filled bands), and external charges so that we have

$$\nabla^2\phi = -4\pi\left(\rho_{\text{carriers}} + \rho_{\text{bound}} + \rho_{\text{external}}\right). \tag{3}$$

In Thomas–Fermi model, the carrier charge density is given by [50]

$$\rho_{\text{carriers}} = -e^2 D\left(E_{\text{Fermi}}\right)\phi, \tag{4}$$

where $D\left(E_{\text{Fermi}}\right)$ is the electronic density of states at the Fermi level. First, let us find the response of carriers to an external charge without the dielectric response of the bound (i.e. we ignore ρ_{ions} for the moment). We find

$$\nabla^2\phi = 4\pi e^2 D\left(E_{\text{Fermi}}\right)\phi - 4\pi\rho_{\text{external}}. \tag{5}$$

Taking the Fourier transform of both sides, we obtain

$$-k^2\tilde{\phi} = 4\pi e^2 D\left(E_{\text{Fermi}}\right)\tilde{\phi} - 4\pi\tilde{\rho}_{\text{external}}, \tag{6}$$

(where tildes denote quantities in Fourier or k space). Rearrangements yield

$$\left(k^2 + k_0^2\right)\tilde{\phi} = 4\pi\tilde{\rho}_{\text{external}}, \tag{7}$$

where $k_0^2 \equiv 4\pi e^2 D\left(E_{\text{Fermi}}\right)$. The screening length is defined as $\lambda_0 = 2\pi/k_0$. For a free electron gas, $D\left(E_{\text{Fermi}}\right)$ is given by $\frac{1}{\pi e^2}\left(\frac{3n}{\pi}\right)^{-\frac{1}{3}}$, where n is the electron density. So the screening length is

$$\lambda_0^2 = \frac{1}{4}\left(\frac{\pi}{3n}\right)^{\frac{1}{3}}. \tag{8}$$

Since we want to find a lower bound for the screening length, we let the density n take its largest possible value in our system. Among the systems we have examined, the one with highest mobile carrier density is the symmetric interface with no capping electrode which has approximately two added electrons per 2×1 unit cell. To further maximize n, we assume the carriers to be concentrated in the first interfacial unit cell of the oxide so that $n \simeq a_{\text{lattice}}^{-3}$. This yields $\lambda_0 \simeq 1$Å.

However, the bound charges in the material will respond to the presence of electric fields. We include this within linear response theory, i.e.

$$\rho_{\text{bound}} = -\nabla\cdot\mathbf{P} = -\nabla\cdot(\chi\mathbf{E}) = \chi\nabla^2\phi, \tag{9}$$

where χ is the electric susceptibility of the bound charges. Including this term in equation (3) modifies equation (5) into

$$\nabla^2\phi = \lambda_0^{-2}\phi - 4\pi\chi\nabla^2\phi - 4\pi\rho_{\text{external}}. \tag{10}$$

Hence the screening length has been modified to

$$\lambda^{-2} = \frac{\lambda_0^{-2}}{1+4\pi\chi} = \frac{\lambda_0^{-2}}{\varepsilon_r}, \tag{11}$$

where ε_r is the relative static dielectric constant of the material. Since bulk BTO has a very large dielectric constant, measurements on thin films of BTO generally yield ε_r of several hundreds [51–53]. However, because we study ultrathin films of BTO (1-4 nm), we conservatively estimate $\varepsilon_r \simeq 50$.

Hence, the screening length of the symmetric interface with no capping electrode is $\lambda_0 \simeq 7$Å. We expect the screening length to be larger for all the other BTO systems we have studied due to their lower carrier densities. Therefore we can safely conclude that screening lengths for these systems are comparable with BTO film thickness which would, in principle, permit configuration switching via an applied electric field.

[1] D. P. Kumah, M. Dogan, J. H. Ngai, D. Qiu, Z. Zhang, D. Su, E. D. Specht, S. Ismail-Beigi, C. H. Ahn, and F. J. Walker, Physical Review Letters **116**, 106101 (2016).

[2] H. Y. Hwang, Y. Iwasa, M. Kawasaki, B. Keimer, N. Nagaosa, and Y. Tokura, Nature Materials **11**, 103 (2012).

[3] J. Mannhart and D. G. Schlom, Science **327**, 1607 (2010).

[4] R. A. McKee, F. J. Walker, and M. F. Chisholm, Science **293**, 468 (2001).

[5] M. Buongiorno Nardelli, F. J. Walker, and R. A. McKee, physica status solidi (b) **241**, 2279 (2004).

[6] J. W. Reiner, F. J. Walker, and C. H. Ahn, Science **323**, 1018 (2009).

[7] R. Droopad, R. Contreras-Guerrero, J. P. Veazey, Q. Qiao, R. F. Klie, and J. Levy, Microelectronic Engineering Insulating Films on Semiconductors 2013, **109**, 290 (2013).

[8] R. A. McKee, F. J. Walker, and M. F. Chisholm, Physical Review Letters **81**, 3014 (1998).

[9] A. Posadas, M. Berg, H. Seo, A. d. Lozanne, A. A. Demkov, D. J. Smith, A. P. Kirk, D. Zhernokletov, and R. M. Wallace, Applied Physics Letters **98**, 053104 (2011).

[10] R. P. Laughlin, D. A. Currie, R. Contreras-Guererro, A. Dedigama, W. Priyantha, R. Droopad, N. Theodoropoulou, P. Gao, and X. Pan, Journal of Applied Physics **113**, 17D919 (2013).

[11] C. Dubourdieu, J. Bruley, T. M. Arruda, A. Posadas, J. Jordan-Sweet, M. M. Frank, E. Cartier, D. J. Frank, S. V. Kalinin, A. A. Demkov, and V. Narayanan, Nature Nanotechnology **8**, 748 (2013).

[12] Z. Li, X. Guo, H.-B. Lu, Z. Zhang, D. Song, S. Cheng, M. Bosman, J. Zhu, Z. Dong, and W. Zhu, Advanced Materials **26**, 7185 (2014).

[13] J. H. Ngai, D. P. Kumah, C. H. Ahn, and F. J. Walker, Applied Physics Letters **104**, 062905 (2014).

[14] P. Ponath, K. Fredrickson, A. B. Posadas, Y. Ren, X. Wu, R. K. Vasudevan, M. Baris Okatan, S. Jesse, T. Aoki, M. R. McCartney, D. J. Smith, S. V. Kalinin, K. Lai, and A. A. Demkov, Nature Communications **6**, 6067 (2015).

[15] C. J. Först, C. R. Ashman, K. Schwarz, and P. E. Blöchl, Nature **427**, 53 (2004).

[16] S. A. Chambers, Y. Liang, Z. Yu, R. Droopad, J. Ramdani, and K. Eisenbeiser, Applied Physics Letters **77**, 1662 (2000).

[17] X. Zhang, A. A. Demkov, H. Li, X. Hu, Y. Wei, and J. Kulik, Physical Review B **68**, 125323 (2003).

[18] A. M. Kolpak, F. J. Walker, J. W. Reiner, Y. Segal, D. Su, M. S. Sawicki, C. C. Broadbridge, Z. Zhang, Y. Zhu, C. H. Ahn, and S. Ismail-Beigi, Physical Review Letters **105**, 217601 (2010).

[19] J. W. Reiner, A. M. Kolpak, Y. Segal, K. F. Garrity, S. Ismail-Beigi, C. H. Ahn, and F. J. Walker, Advanced Materials **22**, 2919 (2010).

[20] W. Zhong, D. Vanderbilt, and K. M. Rabe, Physical Review Letters **73**, 1861 (1994).

[21] F. Amy, A. S. Wan, A. Kahn, F. J. Walker, and R. A. McKee, Journal of Applied Physics **96**, 1635 (2004).

[22] G. Niu, S. Yin, G. Saint-Girons, B. Gautier, P. Lecoeur, V. Pillard, G. Hollinger, and B. Vilquin, Microelectronic Engineering Proceedings of the 17th Biennial International Insulating Films on Semiconductor Conference17th Biennial International Insulating Films on Semiconductor Conference, **88**, 1232 (2011).

[23] C. Merckling, G. Saint-Girons, C. Botella, G. Hollinger, M. Heyns, J. Dekoster, and M. Caymax, Applied Physics Letters **98**, 092901 (2011).

[24] K. D. Fredrickson, P. Ponath, A. B. Posadas, M. R. McCartney, T. Aoki, D. J. Smith, and A. A. Demkov, Applied Physics Letters **104**, 242908 (2014).

[25] L. Kornblum, M. D. Morales-Acosta, E. N. Jin, C. H. Ahn, and F. J. Walker, Advanced Materials Interfaces **2**, n/a (2015).

[26] N. A. Spaldin and M. Fiebig, Science **309**, 391 (2005).

[27] A. Cammarata and J. M. Rondinelli, Physical Review B **87**, 155135 (2013).

[28] J. P. Perdew, K. Burke, and M. Ernzerhof, Physical Review Letters **77**, 3865 (1996).

[29] D. Vanderbilt, Physical Review B **41**, 7892 (1990).

[30] P. Giannozzi, S. Baroni, N. Bonini, M. Calandra, R. Car, C. Cavazzoni, Davide Ceresoli, G. L. Chiarotti, M. Cococcioni, I. Dabo, A. D. Corso, S. d. Gironcoli, S. Fabris, G. Fratesi, R. Gebauer, U. Gerstmann, C. Gougoussis, Anton Kokalj, M. Lazzeri, L. Martin-Samos, N. Marzari, F. Mauri, R. Mazzarello, Stefano Paolini, A. Pasquarello, L. Paulatto, C. Sbraccia, S. Scandolo, G. Sclauzero, A. P. Seitsonen, A. Smogunov, P. Umari, and R. M. Wentzcovitch, Journal of Physics: Condensed Matter **21**, 395502 (2009).

[31] N. Marzari, D. Vanderbilt, A. De Vita, and M. C. Payne, Physical Review Letters **82**, 3296 (1999).

[32] G. Henkelman, B. P. Uberuaga, and H. Jónsson, The Journal of Chemical Physics **113**, 9901 (2000).

[33] L. Bengtsson, Physical Review B **59**, 12301 (1999).

[34] E. A. Stern, Physical Review Letters **93**, 037601 (2004).

[35] Q. Zhang, T. Cagin, and W. A. Goddard, Proceedings of the National Academy of Sciences of the United States of America **103**, 14695 (2006).

[36] P. Ghosez, X. Gonze, and J. P. Michenaud, Ferroelectrics **220**, 1 (1999).

[37] G. H. Kwei, A. C. Lawson, S. J. L. Billinge, and S. W. Cheong, The Journal of Physical Chemistry **97**, 2368 (1993).

[38] M. Needels, M. C. Payne, and J. D. Joannopoulos, Physical Review Letters **58**, 1765 (1987).

[39] M. Needels, M. C. Payne, and J. D. Joannopoulos, Physical Review B **38**, 5543 (1988).

[40] Y. Yoshimoto, Y. Nakamura, H. Kawai, M. Tsukada, and M. Nakayama, Physical Review B **61**, 1965 (2000).

[41] M. K. Hudait, Y. Zhu, N. Jain, D. Maurya, Y. Zhou, R. Varghese, and S. Priya, ACS Applied Materials & Interfaces **5**, 11446 (2013).

[42] P. Tipler and R. Llewellyn, *Modern Physics* (W. H. Freeman, 2003).

[43] D. P. Kumah, A. Malashevich, A. S. Disa, D. A. Arena, F. J. Walker, S. Ismail-Beigi, and C. H. Ahn, Physical Review Applied **2**, 054004 (2014).

[44] A. M. Kolpak and S. Ismail-Beigi, Physical Review B **85**, 195318 (2012).

[45] A. M. Kolpak and S. Ismail-Beigi, Physical Review B **83**, 165318 (2011).

[46] "NIST Chemistry WebBook," .

[47] K. Suzuki and K. Kijima, Japanese Journal of Applied Physics **44**, 2081 (2005).

[48] C. Kittel, *Introduction to Solid State Physics* (Wiley, 2004).

[49] V. I. Anisimov, J. Zaanen, and O. K. Andersen, Physical Review B **44**, 943 (1991).

[50] N. W. Ashcroft and N. D. Mermin, *Solid State Physics* (Holt, Rinehart and Winston, 1976).

[51] T. Hayashi, N. Oji, and H. Maiwa, Japanese Journal of Applied Physics **33**, 5277 (1994).

[52] B. H. Hoerman, G. M. Ford, L. D. Kaufmann, and B. W. Wessels, Applied Physics Letters **73**, 2248 (1998).

[53] O. Trithaveesak, J. Schubert, and C. Buchal, Journal of Applied Physics **98**, 114101 (2005).